Anisotropic spin-wave excitations in multiferroic $BiFeO_3$

Depei Zhang, Sachith Dissanayake,* Barry Winn, and Masaaki Matsuda†
Neutron Scattering Division, Oak Ridge National Laboratory, Oak Ridge, Tennessee 37831, USA

Toshimitsu Ito
National Institute of Advanced Industrial Science and Technology (AIST), Tsukuba, Ibaraki 305-8565, Japan

Randy Fishman
Materials Science and Technology Division, Oak Ridge National Laboratory, Oak Ridge, Tennessee 37831, USA

(Received 8 January 2022; revised 24 March 2022; accepted 4 April 2022; published 21 April 2022)

Polarized inelastic neutron-scattering experiments have been performed to elucidate the anisotropic behavior of the low-energy spin-wave excitations in a multiferroic $BiFeO_3$, which shows a cycloidal spin structure below 640 K. Using neutron polarization analysis for single magnetic domain crystals, magnetic excitation modes in and out of the cycloidal plane below 6 meV were separated successfully. The magnetic excitation spectra were analyzed using linear spin-wave theory. The low-energy magnon density of states consist of several magnon modes, including the two anisotropic modes, Φ and Ψ modes, distributed in and out of the cycloidal plane, respectively, which were previously observed using optical spectroscopies. Furthermore, there are other magnon modes that are not active in optical measurements. A model spin Hamiltonian, which reproduces the spin-wave frequencies observed using optical spectroscopies, explains the overall spectra reasonably well.

DOI: 10.1103/PhysRevB.105.144426

I. INTRODUCTION

Bismuth ferrite $BiFeO_3$ is a multiferroic material that exhibits ferroelectric polarization and antiferromagnetic order above room temperature. The crystal structure is hexagonal $R3c$ with the lattice parameters $a_{\rm hex} \approx 5.58$ Å and $c_{\rm hex} \approx 13.86$ Å below ∼1100 K [1] as shown in Fig. 1(a). The structure can also be represented approximately by the pseudocubic unit cell with the lattice constant $a = a_{\rm pc} \approx 3.96$ Å. This material primarily shows a large spontaneous ferroelectric polarization below 1100 K with an additional polarization below 640 K where a cycloidal magnetic structure develops with the magnetic wave vector $\boldsymbol{q_m} = [\delta, \delta, 3]_{\rm hex}$ ($\delta \approx \frac{1}{222}$) [2–5]. Because this multiferroic behavior occurs above room temperature, extensive studies have been performed to clarify the electromagnetic coupling in this material [6].

One of the interesting features of $BiFeO_3$ is the electromagnon, which is a hybrid mode of magnon and phonon activated by the magnetoelectric coupling. The electromagnon was studied extensively in one of the most celebrated multiferroic systems $R\rm MnO_3$ (R= rare-earth elements) using optical techniques [7]. The nature of the electromagnon depends on the energy range. Low- and high-energy electromagnons are activated by the inverse Dzyaloshinskii-Moriya (DM) coupling [8,9] and exchange-striction mechanisms [10], respectively.

The electromagnon in $BiFeO_3$ was studied using Raman spectroscopy [11–14] and time-resolved terahertz spectroscopy measurements [15,16]. Two kinds of magnon modes (Φ and Ψ modes at lower and higher energies, respectively) were identified. The spectrum has a peaked structure at the crossing points of these magnon modes (Φ_n and Ψ_n with n integers) at the magnetic zone center due to the zone folding. The Φ and Ψ modes correspond to the spin-wave excitations in and out of the cycloidal plane, respectively [17]. The Heisenberg model with a single-ion anisotropy and two kinds of DM interactions successfully explain the electromagnon [$\Psi_1^{(1)}$] and magnetic enhanced [Ψ_0, $\Psi_1^{(2)}$, $\Phi_1^{(1)}$, and $\Phi_2^{(1)}$] modes [18], observed with optical spectroscopies. Due to the electromagnetic coupling, the energies of the magnon modes were found to shift with a changing electric field even at room temperature, indicating the control of spin-wave excitations using an electric field [19].

In principle, the magnon modes reported in the optical spectroscopy measurements can be observed using the inelastic neutron-scattering measurements, which has an advantage of measuring magnon and phonon dispersions over the full range of momentum space, whereas only modes around the zone center can be measured with optical spectroscopies. Therefore, it is important to perform detailed inelastic neutron-scattering measurements in $BiFeO_3$ to study the magnon modes relevant to the electromagnon, although the enhancement of the electromagnon by a photon's electric field cannot be measured. In fact, low-energy magnon modes corresponding to the electromagnon were identified in $DyMnO_3$ and $TbMnO_3$ using inelastic neutron scattering [20,21]. However, there has been no neutron-scattering study

*Present address: Department of Mechanical Engineering, University of Rochester, Rochester, New York 14627, USA.
†Corresponding author: matsudam@ornl.gov

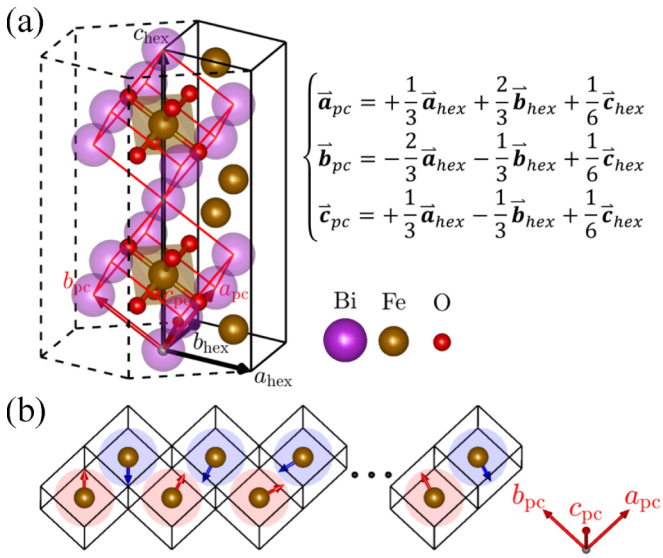

FIG. 1. Crystal and magnetic structures of $BiFeO_3$. (a) The nuclear structure of $BiFeO_3$ where the black and red arrows represent the hexagonal and pseudocubic unit cells, respectively, and the violet, gold, and red spheres represent the Bi, Fe, and O atoms, respectively. The coordinate transformation equations between the hexagonal and pseudocubic cells are listed. (b) The cycloidal magnetic structure of $BiFeO_3$ in the pseudocubic cell where the magnetic wave vector is $\boldsymbol{q_m} = [\delta, \delta, 3]_{\text{hex}}$ with $\delta \approx \frac{1}{222}$, and the cycloidal plane is tilted by $\tau = 0.46^\circ$ from the $[H, H, L]_{\text{hex}}$ plane. Both δ and τ are exaggerated by 20 times for clarification.

in $BiFeO_3$ in this respect. One of the reasons is that the instrumental energy resolution is not sufficient to separate the magnon modes. Even without excellent energy resolution, observing anisotropy of the magnetic excitation modes, which could be feasible using the polarized neutron-scattering technique, would give useful information in identifying magnon modes associated with the electromagnon. However, a crucial issue is the difficulty of identifying the anisotropy of the magnon modes even using the polarized neutron technique because the splitting of the magnetic peaks due to the three magnetic domains is smaller than the instrumental Q resolution. As a result, the anisotropic effect is averaged out completely.

Due to the large spin value and exchange interactions, the magnetic excitation band extends up to ∼70 meV [22,23]. However, the low-energy excitations below ∼6 meV are extremely important to study the magnon modes relevant to the electromagnon in $BiFeO_3$. The low-energy magnetic excitations were measured and analyzed to determine the single-ion anisotropy and the DM interactions in Ref. [24]. Since that neutron-scattering study was performed using a multi-magnetic-domained sample with unpolarized neutrons, the magnetic anisotropy of the magnon modes was not evaluated.

In this paper, two changes to the experimental conditions were made in order to identify the low-energy magnon modes accurately. In particular, we could successfully align the three magnetic domains under high magnetic fields and observe the anisotropy of the magnon modes, i.e., in and out of the cycloidal plane, using the polarized neutron technique. Another important point is that inelastic neutron scattering can observe the magnon modes that are not active in optical measurements. We found that a model spin Hamiltonian, which reproduces the spin-wave frequencies observed using optical spectroscopies [25], explains the overall spectra, including the anisotropy of the magnetic excitations, reasonably well.

II. EXPERIMENTAL DETAILS

A single crystal of $BiFeO_3$ was grown using the traveling solvent floating zone method as described in Ref. [26]. As described in Refs. [27,28], as-grown crystals have three magnetic domains, and the domains can be aligned by applying a magnetic field of 6 T. The domain distribution is preserved as long as the sample is stored at ambient temperature and field. We comounted two single magnetic domained crystals with the dimensions of $3\phi \times 10\ \text{mm}^3$ on the $(HHL)_{\text{hex}}$ scattering plane, which approximately corresponds to the cycloidal plane with a small amount of tilt out of the plane as shown in Fig. 1(b).

Polarized inelastic neutron-scattering measurements were performed on the hybrid neutron spectrometer HYSPEC [29] installed at the Spallation Neutron Source at Oak Ridge National Laboratory. The incident neutron energy E_i was fixed at 7.5 meV to cover the major low-energy part of the magnetic excitations of $BiFeO_3$. The energy resolution is ∼0.4 meV at the elastic position. The incident neutrons were polarized using Heusler (111) crystals, and the polarization of the scattered neutrons was analyzed using wide-angle-arrayed supermirrors. A pair of magnetic coils was used to align the neutron polarization perpendicular to the scattering plane at the sample position. The Mezei spin flipper was used to optionally flip the incident neutron spin. With this setup, the non-spin-flip (NSF) and spin-flip (SF) components were measured with the two-dimensionally arrayed ^{3}He tube detectors. The flipping ratio of this setup was ∼10, estimated using nuclear Bragg peaks, which is consistent with the typical polarization of the instrument with the same configuration. In this configuration, the NSF and SF components correspond to the magnetic contributions out of and in the scattering plane, respectively [30]. The sample table was rotated by ±23° around $(0, 0, 3)_{\text{hex}}$ to measure the excitations in a wide-Q range. Although the phonon signal can be observed at the NSF channel, purely magnetic excitations are expected at the momentum and energy ranges in this paper. Due to the vertical focusing of the incident beam, the instrumental Q resolution out of the scattering plane is much broader than the tilt of the cycloidal plane in the sample. The observed intensities were corrected with the correction factors for the flipping ratio and the transmission of the supermirrors.

Here, the relation between the hexagonal and the pseudocubic structure is described. The hexagonal unit cell of $BiFeO_3$ is shown as the black cell and arrows in Fig. 1(a) where the violet, gold, and red spheres represent the Bi, Fe, and O atoms, respectively. The pseudocubic unit cell is shown as the red cells and arrows. Each pseudocubic unit cell contains one chemical formula unit, whereas the hexagonal cell contains six. The lattice vectors of the hexagonal and pseudocubic cells can be converted using the following

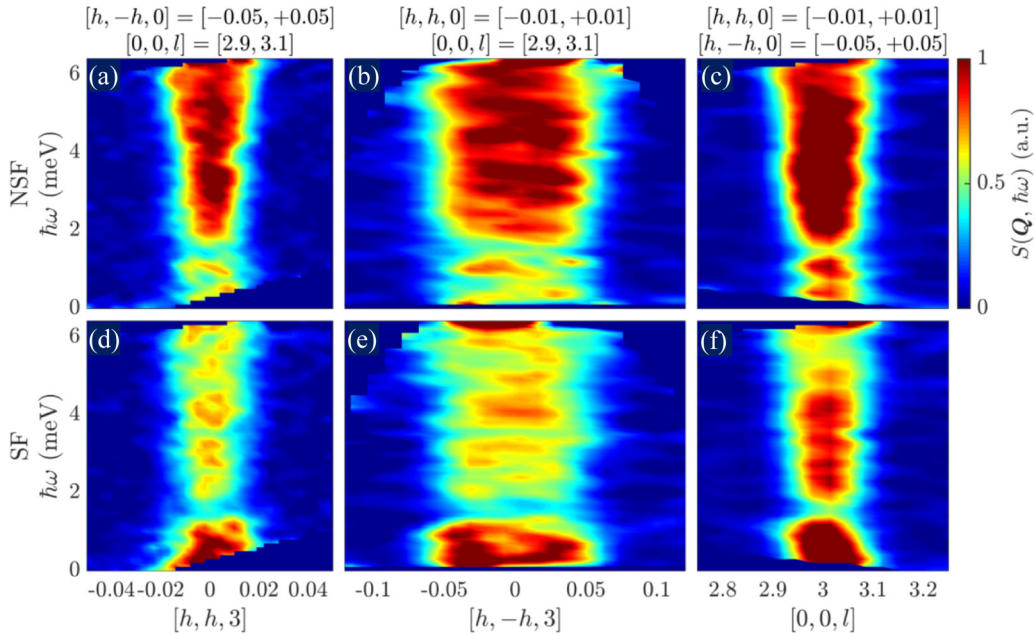

FIG. 2. Contour plots of the polarized inelastic neutron-scattering spectra of $BiFeO_3$ measured at 300 K. Panels (a)–(c) and (d)–(f) show the neutron intensity $S(\boldsymbol{Q}, \hbar\omega)$ as a function of the momentum transfer $\boldsymbol{Q}$ and the energy transfer $\hbar\omega$ for the NSF and SF components, respectively, along three orthogonal directions, $[h, h, 3]_{\text{hex}}$ [(a) and (d)], $[h, -h, 3]_{\text{hex}}$ [(b) and (e)], and $[0, 0, l]_{\text{hex}}$ [(c) and (f)]. In panels (a) and (d), $S(\boldsymbol{Q}, \hbar\omega)$ is integrated over $[h, -h, 0]_{\text{hex}}$ for $-0.05 \leqslant h \leqslant +0.05$ and $[0, 0, l]_{\text{hex}}$ for $2.9 \leqslant l \leqslant 3.1$; in panels (b) and (e), the integration is applied over $[h, h, 0]_{\text{hex}}$ for $-0.01 \leqslant h \leqslant +0.01$ and $[0, 0, l]_{\text{hex}}$ for $2.9 \leqslant l \leqslant 3.1$; whereas in panels (c) and (f), the integration is applied over $[h, h, 0]_{\text{hex}}$ for $-0.01 \leqslant h \leqslant +0.01$ and $[h, -h, 0]_{\text{hex}}$ for $-0.05 \leqslant h \leqslant +0.05$. The counting time for each SF and NSF channel is approximately 40 h. The wider excitations in panels (b) and (e) originate from the broader instrumental Q resolution due to the vertical focusing. The intrinsic width is considered to be similar to that along the two other directions. The observed intensities were corrected with the transmission and the flipping ratio factors.

equations:

$$\begin{aligned}
\boldsymbol{a}_{\text{pc}} &= +\tfrac{1}{3}\boldsymbol{a}_{\text{hex}} + \tfrac{2}{3}\boldsymbol{b}_{\text{hex}} + \tfrac{1}{6}\boldsymbol{c}_{\text{hex}},\\
\boldsymbol{b}_{\text{pc}} &= -\tfrac{2}{3}\boldsymbol{a}_{\text{hex}} - \tfrac{1}{3}\boldsymbol{b}_{\text{hex}} + \tfrac{1}{6}\boldsymbol{c}_{\text{hex}},\\
\boldsymbol{c}_{\text{pc}} &= +\tfrac{1}{3}\boldsymbol{a}_{\text{hex}} - \tfrac{1}{3}\boldsymbol{b}_{\text{hex}} + \tfrac{1}{6}\boldsymbol{c}_{\text{hex}},
\end{aligned} \tag{1}$$

where $\boldsymbol{a}_{\text{pc}}$, $\boldsymbol{b}_{\text{pc}}$, $\boldsymbol{c}_{\text{pc}}$ and $\boldsymbol{a}_{\text{hex}}$, $\boldsymbol{b}_{\text{hex}}$, $\boldsymbol{c}_{\text{hex}}$ represent the lattice vectors for the pseudocubic and hexagonal cells, respectively.

Similarly, we can also obtain the transformation equations for the reciprocal lattice vectors,

$$\begin{aligned}
\boldsymbol{a}^*_{\text{pc}} &= +\boldsymbol{b}^*_{\text{hex}} + 2\boldsymbol{c}^*_{\text{hex}},\\
\boldsymbol{b}^*_{\text{pc}} &= -\boldsymbol{a}^*_{\text{hex}} + 2\boldsymbol{c}^*_{\text{hex}},\\
\boldsymbol{c}^*_{\text{pc}} &= +\boldsymbol{a}^*_{\text{hex}} - \boldsymbol{b}^*_{\text{hex}} + 2\boldsymbol{c}^*_{\text{hex}},
\end{aligned} \tag{2}$$

where $\boldsymbol{a}^*_{\text{pc}}$, $\boldsymbol{b}^*_{\text{pc}}$, $\boldsymbol{c}^*_{\text{pc}}$ and $\boldsymbol{a}^*_{\text{hex}}$, $\boldsymbol{b}^*_{\text{hex}}$, $\boldsymbol{c}^*_{\text{hex}}$ represent the reciprocal lattice vectors for the pseudocubic and hexagonal cells, respectively.

Therefore, the $[1, 1, 0]_{\text{hex}} - [0, 0, 1]_{\text{hex}}$ scattering plane corresponds to the $[1, -1, 0]_{\text{pc}} - [1, 1, 1]_{\text{pc}}$ plane, and the polarization direction of $[1, -1, 0]_{\text{hex}}$ corresponds to $[-1, -1, 2]_{\text{pc}}$. The hexagonal notation will mostly be used in this paper, and the equivalent values for the pseudocubic notation will be shown at some places. We will also use $\boldsymbol{x}'$, $\boldsymbol{y}'$, and $\boldsymbol{z}'$, which are defined as unit vectors along $[1, 1, 0]_{\text{hex}}$, $[1, -1, 0]_{\text{hex}}$, and $[0, 0, 1]_{\text{hex}}$, respectively.

III. RESULTS AND DISCUSSION

A. Polarized inelastic neutron-scattering experiments

Figure 2 shows the polarized inelastic neutron-scattering spectra of $BiFeO_3$ measured at 300 K along three orthogonal reciprocal directions in the vicinity of $(0, 0, 3)_{\text{hex}}$, which is close to the magnetic wave-vector $\boldsymbol{q_m} = [\delta, \delta, 3]_{\text{hex}}$. Although the incommensurate magnetic peaks are present at $(\delta, \delta, 3)_{\text{hex}}$, the instrumental Q resolution is not sufficient to resolve the detailed structure in the momentum space. The magnetic excitation spectra clearly show that both the NSF and the SF components exhibit a gap at $\hbar\omega \approx 1.5$ meV and the NSF component mainly contributes to the magnetic excitations above the gap, whereas the SF signals are mainly distributed below the gap.

In order to show the anisotropic behavior of the magnetic excitations more clearly, the NSF and SF components of the magnetic excitations are displayed as a function of excitation energy around $(0, 0, 3)_{\text{hex}}$ in Fig. 3. The experimental intensity $S_{\text{exp}}(\hbar\omega)$ is integrated over $[h, h, 0]_{\text{hex}}$ for $-0.01 \leqslant h \leqslant +0.01$, $[h, -h, 0]_{\text{hex}}$ for $-0.05 \leqslant h \leqslant +0.05$, and $[0, 0, l]_{\text{hex}}$ for $2.9 \leqslant l \leqslant 3.1$. The NSF and SF components mainly contribute to the magnetic excitations above and below ∼1.5 meV, respectively. This indicates that the out-of-plane and in-plane spin-wave modes are largely populated above and below the gap, respectively. The shape of the overall low-energy magnetic excitations are similar to that measured with unpolarized neutrons in Ref. [24], considering that the result

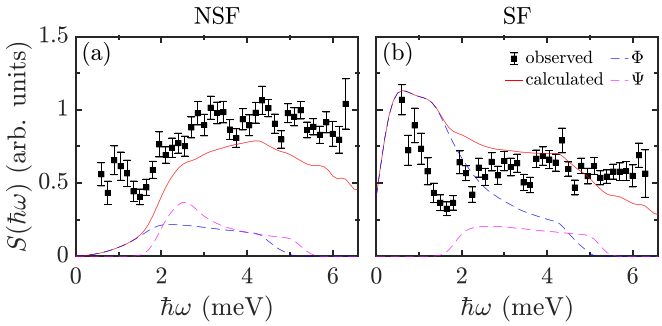

FIG. 3. Energy dependence of the magnetic excitations of $BiFeO_3$ measured with polarized neutrons. The NSF and SF components correspond to the magnetic excitations out of and in the cycloidal plane, respectively. Panels (a) and (b) compare the experimental and calculated spin-wave intensities for the NSF and SF components, respectively. The filled squares show the $\boldsymbol{Q}$-integrated neutron intensity $S_{\rm exp}(\hbar\omega) = \int d^3\boldsymbol{Q} S_{\rm exp}(\boldsymbol{Q}, \hbar\omega)$, obtained from the experimental results displayed in Fig. 2 where the integration is applied over $[h, h, 0]_{\rm hex}$ for $-0.01 \leqslant h \leqslant +0.01$, $[h, -h, 0]_{\rm hex}$ for $-0.05 \leqslant h \leqslant +0.05$ and $[0, 0, l]_{\rm hex}$ for $2.9 \leqslant l \leqslant 3.1$. The red solid line represents the calculated $\hbar\omega$ dependence of spin-wave intensity $S_{\rm calc}(\hbar\omega)$. The $S_{\rm calc}(\hbar\omega)$ is integrated over the the $\boldsymbol{Q}$ points in the vicinity of $(0, 0, 3)_{\rm hex}$ considering the experimental $\boldsymbol{Q}$ resolution, which integrates most of the spin-wave excitations in the energy range. The blue and magenta dashed lines show the spin-wave mode contribution of $S_{\rm calc}(\hbar\omega)$ from the Φ and Ψ modes, respectively [18]. The excitation signal below 0.5 meV containing the elastic component is not shown.

in Ref. [24] corresponds to the sum of the NSF and SF components.

B. Linear spin-wave calculations

The spin Hamiltonian and ground state for the spin state of $BiFeO_3$ are described in Ref. [18]. The Hamiltonian $\mathcal{H}$ has five terms: the nearest-neighbor (NN), next-nearest-neighbor (NNN), and anisotropic exchange interactions J_1, J_2, and K, respectively, and two DM interactions with $\boldsymbol{D} \parallel [1, -1, 0]_{\rm hex}$ and $\boldsymbol{D'} \parallel [0, 0, 1]_{\rm hex}$,

$$\begin{aligned}\mathcal{H} = &-J_1 \sum_{\rm NN} \boldsymbol{S}_i \cdot \boldsymbol{S}_j - J_2 \sum_{\rm NNN} \boldsymbol{S}_i \cdot \boldsymbol{S}_j \\ &- K \sum_i S_{iz'}^2 - \boldsymbol{D} \cdot \sum_{\langle i,j \rangle} (\boldsymbol{S}_i \times \boldsymbol{S}_j) \\ &- \boldsymbol{D'} \cdot \sum_{\langle i,j \rangle} (-1)^{6R_{iz'}/c} (\boldsymbol{S}_i \times \boldsymbol{S}_j), \end{aligned} \tag{3}$$

where $\boldsymbol{R}_i$ and $\boldsymbol{S}_i$ are the spatial position and the spin orientation of the ith spin, respectively. The sums for the two DM terms run over the NNs. For the second DM term, the sign changes from layer n to layer $n + 1$ along the c axis. The first DM term gives rise to the cycloid modulation. The second DM term causes a small spin-density wave component along $[1, -1, 0]_{\rm hex}$, which tilts the cycloidal plane. Since the Fe^{3+} spin is large ($S = 5/2$), a $1/S$ linear expansion about the classical limit is justified for $BiFeO_3$. This expansion produces a spectrum of observed in-plane and out-of-plane cycloidal modes that agree very well with spectroscopic measurements [25].

The magnetic ground state of the Fe^{3+} spins shows a cycloidal structure with $\boldsymbol{q_m} = [\delta, \delta, 3]_{\rm hex}\{= [0.5 + \delta, 0.5 - \delta, 0.5]_{\rm pc}\}$ ($\delta \approx \frac{1}{222}$) in which the cycloidal plane lies approximately in the $\boldsymbol{x'} - \boldsymbol{z'}$ plane with a tilting angle $\tau (= 0.46^\circ)$. The spin components of the Fe^{3+} ions at $\boldsymbol{R}$, $S(\boldsymbol{R})$, can be expressed as

$$\begin{aligned} S_{x'}(\boldsymbol{R}) &= (-1)^{6R_{z'}/c} \cos\tau \sqrt{S^2 - S_{z'}(\boldsymbol{R})^2}\, \mathrm{sgn}[\sin(2\pi\delta R_{x'}/a)], \\ S_{y'}(\boldsymbol{R}) &= \sin\tau \sqrt{S^2 - S_{z'}(\boldsymbol{R})^2}\, \mathrm{sgn}[\sin(2\pi\delta R_{x'}/a)], \\ S_{z'}(\boldsymbol{R}) &= (-1)^{6R_{z'}/c} S \sum_{m=0}^{\infty} C_{2m+1} \cos[(2m+1)2\pi\delta R_{x'}/a], \end{aligned} \tag{4}$$

where C_{2m+1} are the odd-order cosine coefficients, which satisfy $\sum_{m=0}^{\infty} C_{2m+1} = 1$.

In order to understand the nature of the magnetic excitations and to reproduce the observed polarized spectra, the spin-wave energies and intensities of $BiFeO_3$ are calculated using the equations-of-motion technique for noncollinear spins [31] on a pseudocommensurate magnetic supercell containing $M = 2/\delta = 2 \times 222$ pseudocubic cells [18]. The exchange interactions used for our analysis are $J_1 = -5.32$, $J_2 = -0.24$, $K = 0.005$, $D = 0.18$, and $D' = 0.085$ meV, which reproduce the spin-wave frequencies in zero and finite magnetic fields [25]. Based on these parameters, the magnetic ground state then can be determined: the cycloidal plane tilting angle $\tau = 0.46^\circ$ and the cosine coefficients $C_1 = 1.049\,275$, $C_3 = -0.051\,811$, $C_5 = 0.002\,536$, where the higher-order coefficients are fixed at zero. The linear spin-wave calculations in the vicinity of $\boldsymbol{q_m}$ are shown in Figs. 4 and 5 where the $\boldsymbol{Q}$ space centers are located at $(0, 0, 3)_{\rm hex}$ and $(\delta, \delta, 3)_{\rm hex}$, respectively.

As expected from the cycloidal spin structure, the magnetic dispersions has a periodicity of 2δ along the $[h, h, 0]_{\rm hex}$ direction, whereas the dispersions perpendicular to the $[h, h, 0]_{\rm hex}$ direction are more straightforward. The magnetic excitations emerging from $(0, 0, 3)_{\rm hex}$, shown in Fig. 4, indicate that both the NSF and the SF components are weak in the gapless mode and the gapped modes with minimum at $\sim$2 meV are intense both in the NSF and the SF components. On the other hand, the magnetic excitations emerging from $(\delta, \delta, 3)_{\rm hex}$, shown in Fig. 5, indicate that the gapless mode is more intense in the SF component than in the NSF component and the gapped mode with minimum at $\sim$2.5 meV is more intense in the NSF component than in the SF component. As described in Sec. III A, those magnon modes at $(0, 0, 3)_{\rm hex}$ and $(\delta, \delta, 3)_{\rm hex}$ cannot be resolved and the magnetic excitations integrated over finite momentum and energy ranges are observed experimentally.

The calculated $S_{\rm calc}(\hbar\omega)$ as represented with solid and dashed curves in Fig. 3 is integrated over the $\boldsymbol{Q}$ points in the vicinity of $(0, 0, 3)_{\rm hex}$ in the following way. As seen from Figs. 4 and 5, $S(\boldsymbol{Q}, \hbar\omega)$ shows an approximate cylindrical symmetry where the longitudinal axis is along the $\boldsymbol{x'}$ axis $\{= [1, 1, 0]_{\rm hex}\}$, and the reference plane aligns with the $(\boldsymbol{y'} - \boldsymbol{z'}\{= [1, -1, 0]_{\rm hex} - [0, 0, 1]_{\rm hex}\})$ plane. Therefore, the integrated intensity $S_{\rm calc}(\hbar\omega)$ can be approximated as

$$\begin{aligned} S_{\rm calc}(\hbar\omega) &= \int d^3\boldsymbol{Q}\, S_{\rm calc}(\boldsymbol{Q}, \hbar\omega) \\ &= \int d\eta \int \xi\, d\xi\, S_{\rm calc}(\xi, \eta, \hbar\omega), \end{aligned} \tag{5}$$

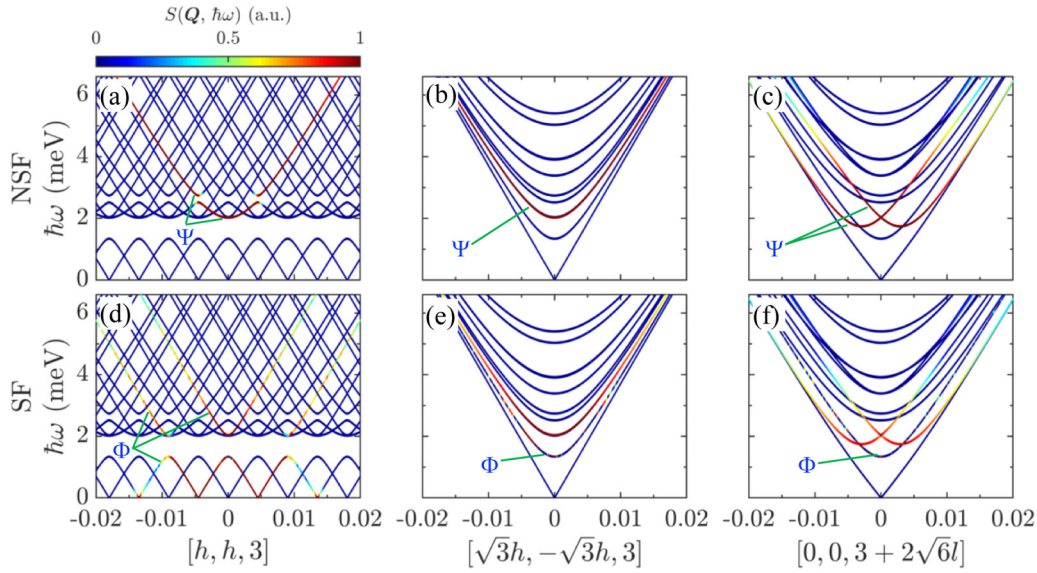

FIG. 4. Magnetic dispersion relations in the vicinity of $(0, 0, 3)_{\text{hex}}$ calculated using the linear spin wave theory for $BiFeO_3$. The spin wave energies and intensities were calculated using the equations-of-motion technique for noncollinear spins [31] on a pseudocommensurate magnetic supercell containing $M = 2 \times 222$ pseudocubic cells [18]. Panels (a)–(c) and (d)–(f) show the calculated spin-wave intensity, $S(\boldsymbol{Q}, \hbar\omega)$, as a function of the momentum transfer $\boldsymbol{Q}$ and the energy transfer $\hbar\omega$ for the NSF and SF components, respectively, along three orthogonal directions, $[h, h, 3]_{\text{hex}}$, $[\sqrt{3}h, -\sqrt{3}h, 3]_{\text{hex}}$, and $[0, 0, 3 + 2\sqrt{6}l]_{\text{hex}}$, which are consistent with the geometry used in Fig. 2. The wave-vector components h and l are rescaled so that they display the equivalent unit in the horizontal axis.

where η, representing the coordinate along the longitudinal axis, is along $\boldsymbol{x}'$, and ξ represents the coordinate along an arbitrary polar axis $\boldsymbol{\xi}$, which is within the reference plane $\boldsymbol{y}' - \boldsymbol{z}'$. $S_{\text{calc}}(\hbar\omega)$ is averaged over three $\boldsymbol{\xi}$ orientations, i.e., $\boldsymbol{z}'$, $\boldsymbol{y}' + \boldsymbol{z}'$, and $\boldsymbol{y}' - 2\boldsymbol{z}'$. Then, the integral is taken over $-0.02 \leqslant \eta \leqslant +0.02$ and $0 \leqslant \xi \leqslant +0.02$ to include most of the spin-wave excitations below 6 meV (Figs. 4 and 5) as the instrumental $\boldsymbol{Q}$ resolution integrates experimentally. Finally, the instrumental energy resolution is convoluted with the $\boldsymbol{Q}$ integrated excitation data.

As shown in Fig. 3, the observed NSF and SF components are more intense above and below ∼1.5 meV, respectively. The calculated NSF and SF components reproduce the overall feature of the observed ones reasonably well, although the detailed structure cannot be fully reproduced. In particular, a dip observed around 1.8 meV, possibly corresponding to the gap around 1.8 meV, shown in Figs. 5(a) and 5(d), is not reproduced. This is partly because the calculated intensities are not integrated perfectly well. The interaction parameters might need to be adjusted in order to obtain better agreement

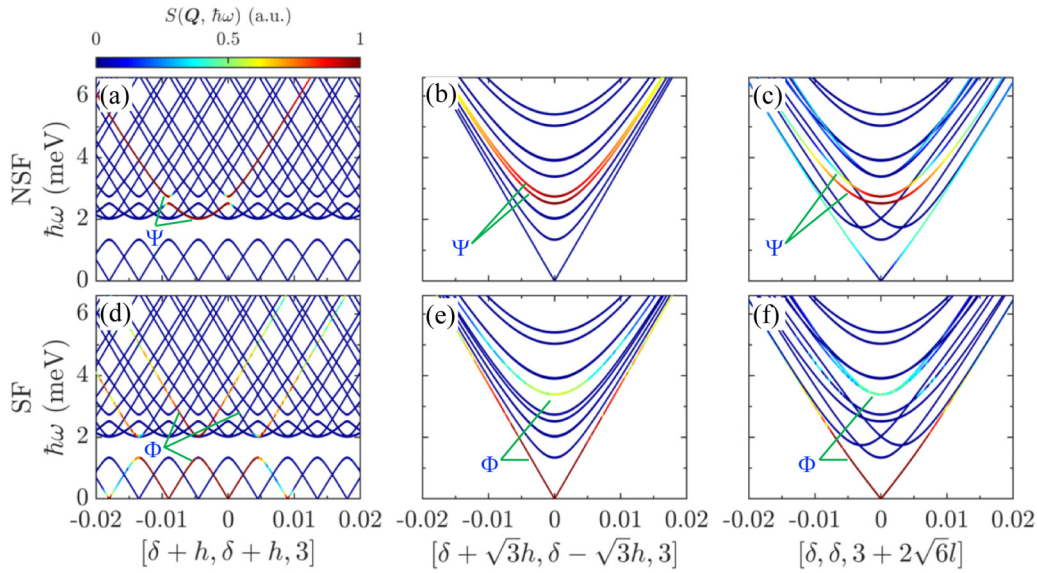

FIG. 5. Magnetic dispersion relations in the vicinity of $(\delta, \delta, 3)_{\text{hex}}$ calculated using the linear spin-wave theory for $BiFeO_3$. Panels (a)–(c) and (d)–(f) show the calculated spin-wave intensity $S(\boldsymbol{Q}, \hbar\omega)$ for the NSF and SF components, respectively, along three orthogonal directions, $[\delta + h, \delta + h, 3]_{\text{hex}}$, $[\delta + \sqrt{3}h, \delta - \sqrt{3}h, 3]_{\text{hex}}$, and $[\delta, \delta, 3 + 2\sqrt{6}l]_{\text{hex}}$.

between the experimental and calculated results. However, the integration of the calculated intensities over the wide momentum and energy ranges requires intense effort. Therefore, the refinement of the parameters is beyond the scope of this paper. Another puzzling feature is that the NSF intensities observed below ∼1.5 meV are much larger than those calculated as shown in Fig. 3(a). Although there may be some contributions, originating from a small fraction of misoriented magnetic domains, the intensities are supposed to be minor. In principle, there can be phonon contribution in the NSF channel. However, the phonon contribution is considered to be absent since the $(\delta, \delta, 3)_{\mathrm{hex}}$ Bragg peaks are purely magnetic in origin, and acoustic phonons at low energies are not expected. Further study is required to clarify this issue.

Here, let us look into the magnetic excitations in more detail. The observed spin excitations of $BiFeO_3$ break down into two classes. Class Φ are in-plane cycloidal modes that roughly correspond to rotations of the spin in the cycloidal plane defined by the propagation vector $\boldsymbol{q_m}$ and the polarization direction z'. This class includes a Goldstone mode that requires no energy. The other class Ψ corresponds to out-of-plane rotations that correspond to oscillations primarily in the direction $\boldsymbol{q_m} \times z'$. As described in Sec. I, the two magnon modes Φ and Ψ were reported from the optical spectroscopy measurements [11,15–17]. In Figs. 4 and 5, Φ and Ψ modes are indicated among the calculated magnon modes. The Φ mode emerges from the zero energy and has a gap around 1.8 meV. The Ψ mode is a gapped mode with a gap energy of ∼2 meV. In Figs. 3(a) and 3(b), the calculated Φ and Ψ mode intensities are exhibited separately. The Φ mode is predicted mostly in the SF channel, corresponding to the easy-plane anisotropy within the cycloidal plane. On the other hand, the Ψ mode, which emerges above ∼2 meV, has larger contribution to the NSF channel, corresponding to the easy-axis anisotropy out of the cycloidal plane. As shown in Figs. 4(c) and 4(f), this mode has a non-negligible contribution to the SF channel. Above ∼2.5 meV, there is a large amount of contributions to both the SF and the NSF channels from other excitation modes, which are predicted to be isotropic.

Mode $\Psi_1^{(1)}$ at ∼2.7 meV was identified to be the electromagnon in Ref. [18]. In our inelastic neutron measurements, a major part of the Ψ mode corresponds to the shoulder around 2.5 meV in the NSF channel. Therefore, this out-of-plane mode is considered to be enhanced by the photon's electric field. Besides the anisotropic Φ and Ψ modes, which have electromagnon and magnetic resonance characters, other magnon modes are found to be isotropic.

IV. CONCLUSION

Using the polarized inelastic neutron-scattering technique with single magnetic domained crystals, the magnetic excitation modes distributed in and out of the cycloidal plane have been observed separately in $BiFeO_3$. The theoretical calculations using the linear spin-wave theory identified the anisotropic and isotropic spin-wave excitation modes, which can explain the overall experimental results reasonably well. Our results provide important information on how the magnetic excitations, in particular, Φ and Ψ modes, observed by optical and neutron-scattering spectroscopies are related.

ACKNOWLEDGMENTS

R.F. acknowledges support by the U.S. Department of Energy, Office of Basic Energy Sciences, Materials Sciences and Engineering Division. This research used resources at the Spallation Neutron Source, a DOE Office of Science User Facility operated by the Oak Ridge National Laboratory. This work was supported by the Paul Scherrer Institut by providing the supermirror analyzer as a temporary loan to Oak Ridge National Laboratory.

[1] J. Moreau, C. Michel, R. Gerson, and W. James, Ferroelectric $BiFeO_3$ X-ray and neutron diffraction study, J. Phys. Chem. Solids **32**, 1315 (1971).

[2] I. Sosnowska, T. P. Neumaier, and E. Steichele, Spiral magnetic ordering in bismuth ferrite, J. Phys. C: Solid State Phys. **15**, 4835 (1982).

[3] J. Herrero-Albillos, G. Catalan, J. A. Rodriguez-Velamazan, M. Viret, D. Colson, and J. F. Scott, Neutron diffraction study of the $BiFeO_3$ spin cycloid at low temperature, J. Phys.: Condens. Matter **22**, 256001 (2010).

[4] M. Ramazanoglu, W. Ratcliff, Y. J. Choi, S. Lee, S.-W. Cheong, and V. Kiryukhin, Temperature-dependent properties of the magnetic order in single-crystal $BiFeO_3$, Phys. Rev. B **83**, 174434 (2011).

[5] I. Sosnowska and R. Przeniosło, Low-temperature evolution of the modulated magnetic structure in the ferroelectric antiferromagnet $BiFeO_3$, Phys. Rev. B **84**, 144404 (2011).

[6] J.-G. Park, M. D. Le, J. Jeong, and S. Lee, Structure and spin dynamics of multiferroic $BiFeO_3$, J. Phys.: Condens. Matter **26**, 433202 (2014).

[7] M. Mochizuki, N. Furukawa, and N. Nagaosa, Theory of Electromagnons in the Multiferroic Mn Perovskites: The Vital Role of Higher Harmonic Components of the Spiral Spin Order, Phys. Rev. Lett. **104**, 177206 (2010).

[8] H. Katsura, A. V. Balatsky, and N. Nagaosa, Dynamical Magnetoelectric Coupling in Helical Magnets, Phys. Rev. Lett. **98**, 027203 (2007).

[9] Y. Takahashi, R. Shimano, Y. Kaneko, H. Murakawa, and Y. Tokura, Magnetoelectric resonance with electromagnons in a perovskite helimagnet, Nat. Phys. **8**, 121 (2012).

[10] R. Valdés Aguilar, M. Mostovoy, A. B. Sushkov, C. L. Zhang, Y. J. Choi, S.-W. Cheong, and H. D. Drew, Origin of Electromagnon Excitations in Multiferroic $R\mathrm{MnO}_3$, Phys. Rev. Lett. **102**, 047203 (2009).

[11] M. Cazayous, Y. Gallais, A. Sacuto, R. de Sousa, D. Lebeugle, and D. Colson, Possible Observation of Cycloidal Electromagnons in $BiFeO_3$, Phys. Rev. Lett. **101**, 037601 (2008).

[12] P. Rovillain, M. Cazayous, Y. Gallais, A. Sacuto, R. P. S. M. Lobo, D. Lebeugle, and D. Colson, Polar phonons and spin excitations coupling in multiferroic $BiFeO_3$ crystals, Phys. Rev. B **79**, 180411(R) (2009).

[13] M. K. Singh, R. S. Katiyar, and J. F. Scott, New magnetic phase transitions in $BiFeO_3$, J. Phys.: Condens. Matter **20**, 252203 (2008).

[14] J. F. Scott, M. K. Singh, and R. S. Katiyar, Critical phenomena at the 140 and 200 K magnetic phase transitions in $BiFeO_3$, J. Phys.: Condens. Matter **20**, 322203 (2008).

[15] D. Talbayev, S. A. Trugman, S. Lee, H. T. Yi, S.-W. Cheong, and A. J. Taylor, Long-wavelength magnetic and magnetoelectric excitations in the ferroelectric antiferromagnet $BiFeO_3$, Phys. Rev. B **83**, 094403 (2011).

[16] U. Nagel, R. S. Fishman, T. Katuwal, H. Engelkamp, D. Talbayev, H. T. Yi, S.-W. Cheong, and T. Rõõm, Terahertz Spectroscopy of Spin Waves in Multiferroic $BiFeO_3$ in High Magnetic Fields, Phys. Rev. Lett. **110**, 257201 (2013).

[17] R. de Sousa and J. E. Moore, Optical coupling to spin waves in the cycloidal multiferroic $BiFeO_3$, Phys. Rev. B **77**, 012406 (2008).

[18] R. S. Fishman, J. T. Haraldsen, N. Furukawa, and S. Miyahara, Spin state and spectroscopic modes of multiferroic $BiFeO_3$, Phys. Rev. B **87**, 134416 (2013).

[19] P. Rovillain, R. de Sousa, Y. Gallais, A. Sacuto, M. A. Méasson, D. Colson, A. Forget, M. Bibes, A. Barthélémy, and M. Cazayous, Electric-field control of spin waves at room temperature in multiferroic $BiFeO_3$, Nature Mater. **9**, 975 (2010).

[20] T. Finger, K. Binder, Y. Sidis, A. Maljuk, D. N. Argyriou, and M. Braden, Magnetic order and electromagnon excitations in $DyMnO_3$ studied by neutron scattering experiments, Phys. Rev. B **90**, 224418 (2014).

[21] S. Holbein, P. Steffens, T. Finger, A. C. Komarek, Y. Sidis, P. Link, and M. Braden, Field and temperature dependence of electromagnon scattering in $TbMnO_3$ studied by inelastic neutron scattering, Phys. Rev. B **91**, 014432 (2015).

[22] J. Jeong, E. A. Goremychkin, T. Guidi, K. Nakajima, G. S. Jeon, S.-A. Kim, S. Furukawa, Y. B. Kim, S. Lee, V. Kiryukhin, S.-W. Cheong, and J.-G. Park, Spin Wave Measurements Over the Full Brillouin Zone of Multiferroic $BiFeO_3$, Phys. Rev. Lett. **108**, 077202 (2012).

[23] M. Matsuda, R. S. Fishman, T. Hong, C. H. Lee, T. Ushiyama, Y. Yanagisawa, Y. Tomioka, and T. Ito, Magnetic Dispersion and Anisotropy in Multiferroic $BiFeO_3$, Phys. Rev. Lett. **109**, 067205 (2012).

[24] J. Jeong, M. D. Le, P. Bourges, S. Petit, S. Furukawa, S.-A. Kim, S. Lee, S.-W. Cheong, and J.-G. Park, Temperature-Dependent Interplay of Dzyaloshinskii-Moriya Interaction and Single-Ion Anisotropy in Multiferroic $BiFeO_3$, Phys. Rev. Lett. **113**, 107202 (2014).

[25] R. S. Fishman, J. H. Lee, S. Bordács, I. Kézsmárki, U. Nagel, and T. Rõõm, Spin-induced polarizations and nonreciprocal directional dichroism of the room-temperature multiferroic $BiFeO_3$, Phys. Rev. B **92**, 094422 (2015).

[26] T. Ito, T. Ushiyama, Y. Yanagisawa, R. Kumai, and Y. Tomioka, Growth of highly insulating bulk single crystals of multiferroic $BiFeO_3$ and their inherent internal strains in the domain-switching process, Cryst. Growth Des. **11**, 5139 (2011).

[27] S. Kawachi, A. Miyake, T. Ito, S. E. Dissanayake, M. Matsuda, W. Ratcliff, Z. Xu, Y. Zhao, S. Miyahara, N. Furukawa, and M. Tokunaga, Successive field-induced transitions in $BiFeO_3$ around room temperature, Phys. Rev. Mater. **1**, 024408 (2017).

[28] M. Matsuda, S. E. Dissanayake, T. Hong, Y. Ozaki, T. Ito, M. Tokunaga, X. Z. Liu, M. Bartkowiak, and O. Prokhnenko, Magnetic field induced antiferromagnetic cone structure in multiferroic $BiFeO_3$, Phys. Rev. Mater. **4**, 034412 (2020).

[29] I. A. Zaliznyak, A. T. Savici, V. O. Garlea, B. Winn, U. Filges, J. Schneeloch, J. M. Tranquada, G. Gu, A. Wang, and C. Petrovic, Polarized neutron scattering on HYSPEC: the HYbrid SPECtrometer at SNS, J. Phys.: Conf. Ser. **862**, 012030 (2017).

[30] W. G. Williams, *Polarized Neutrons* (Oxford Science, Oxford, 1988).

[31] J. T. Haraldsen and R. S. Fishman, Spin rotation technique for non-collinear magnetic systems: Application to the generalized villain model, J. Phys.: Condens. Matter **21**, 216001 (2009).